

PAPER

Realization of topological Bragg and locally resonant interface states in one-dimensional metamaterial beam-resonator-foundation system

To cite this article: Hanqing Zhang *et al* 2024 *J. Phys. D: Appl. Phys.* **57** 505304

View the [article online](#) for updates and enhancements.

You may also like

- [A sonic band gap based on the locally resonant phononic plates with stubs](#)
Mourad Oudich, Yong Li, Badreddine M Assouar et al.
- [Flexural wave band gaps in metamaterial beams with membrane-type resonators: theory and experiment](#)
Hao Zhang, Yong Xiao, Jihong Wen et al.
- [Response characteristics of vegetation and soil environment to permafrost degradation in the upstream regions of the Shule River Basin](#)
Shengyun Chen, Wenjie Liu, Xiang Qin et al.



The ECS United logo features a large green circle containing the text "ECS UNITED" in white, curved along the top edge. Inside the circle, there are three light blue diagonal bars forming a stylized "U" shape.

ECS The Electrochemical Society
Advancing solid state & electrochemical science & technology

247th ECS Meeting
Montréal, Canada
May 18-22, 2025
Palais des Congrès de Montréal

Showcase your science!

Abstracts due December 6th

Realization of topological Bragg and locally resonant interface states in one-dimensional metamaterial beam-resonator-foundation system

Hanqing Zhang^{1,3,4} , Lihua Tang⁴ , Guobiao Hu⁵ , Yingli Li^{1,2,3,*}  and Kean Aw⁴

¹ Key Laboratory of Traffic Safety on Track (Central South University), Ministry of Education, School of Traffic and Transportation Engineering, Central South University, Changsha 410075, People's Republic of China

² Joint International Research Laboratory of Key Technology for Rail Traffic Safety, Central South University, Changsha 410075, People's Republic of China

³ National and Local Joint Engineering Research Centre of Safety Technology for Rail Vehicle, Central South University, Changsha 410075, People's Republic of China

⁴ Department of Mechanical and Mechatronics Engineering, The University of Auckland, Auckland 1010, New Zealand

⁵ Thrust of the Internet of Things, The Hong Kong University of Science and Technology, Guangzhou, Guangdong 511400, People's Republic of China

E-mail: liyingli@csu.edu.cn

Received 15 July 2024, revised 23 August 2024

Accepted for publication 16 September 2024

Published 1 October 2024



Abstract

In this study, the one-dimensional (1D) metamaterial beam-foundation system is innovatively improved into a metamaterial beam-resonator-foundation system by inserting resonators into the elastic foundation for ultra-low frequency vibration attenuation and enhanced topological energy trapping. Abundant band gap characteristics are obtained including quasi-static band gap starting from 0 Hz, Bragg scattering band gaps (BSBGs), and local resonance band gaps (LRBGs). Five band folding points are obtained through the band folding mechanism which can be opened by tuning inner and outer resonance parameters. However, only three band folding induced band gaps support mode inversion and Zak phase transition, including one BSBG and two LRBGs. The topological inversion in LRBGs is rarely reported in the 1D mechanical system, which can induce topological locally resonant interface states. The underlying physical mechanism of the topological phase transition in LRBG is revealed, which results from the topological inversion band gap transition from an initial BSBG to a LRBG with resonance parameters changes. Different from conventional 1D topological metamaterials that merely utilize local resonance to lower the band frequency and achieve subwavelength topological states in BSBGs, the topological interface states in LRBGs can localize wave energy to fewer unit cells near the interface, exhibiting enhanced energy localization capacity. The topologically protected interface states are validated with defective cases, demonstrating the potential of topological metamaterials for robust energy harvesting. This study provides new insights into the topological theory of 1D mechanical systems and contributes to the development and implementation of multi-functional devices integrating vibration attenuation and energy trapping.

* Author to whom any correspondence should be addressed.

Keywords: metamaterial beam-resonator-foundation system, band gap mechanism, topological interface state, local resonance, energy localization

1. Introduction

Over the past two decades, various types of metamaterials have been constantly proposed to achieve the special properties not found in natural materials [1–3]. Due to the unique band gap characteristics [4–6], the periodic mechanical metamaterials constructed by engineering microstructures and arranging local resonators can effectively suppress vibrations in low-frequency regimes, opening up a new avenue for vibration control and wave manipulation. Recently, as an extension of the concept of topological insulators in condensed matter physics, topological metamaterials have aroused considerable attention in the classic mechanical system [7, 8], which have demonstrated unprecedented wave manipulation capabilities and energy localization effects that are immune to structural defects and perturbations. These distinctive characteristics originate from the topologically protected states within topological band gaps, enabling topological metamaterials as multi-functional devices beyond vibration attenuation application, such as waveguides [9, 10], logic gates [11, 12], energy harvesting [13, 14], microparticle separation [15], etc.

In one-dimensional (1D) mechanical topological systems, topologically protected interface states are the modes of great signification, which appear at the interface constructed by two topologically different unit cells [16, 17]. The different topological properties of topological band gaps guarantee the intensive energy concentration effect at the interface, which is immune to structural defects and disorders [18]. Analogous to the Su–Schrieffer–Heeger model [19], Yin *et al* [20] developed a 1D topological phononic crystal that corresponds to a beam structure with periodically varying cross-sections and studied the topological properties of the 1D beam system for both longitudinal and bending waves. Inspired by their work, similar 1D topological beam structures have been developed by modulating beam sections to break structure spatial symmetry [21–23]. Furthermore, various piezoelectric phononic crystal beams have been proposed to achieve actively-tuned topologically protected wave propagation including both capacitance [24, 25] and inductance [26] modulation methods.

In earlier research, the topological interface states are obtained in relatively high-frequency band gaps originating from the Bragg scattering mechanism. To achieve the topological interface state in the subwavelength frequency range, Zhao *et al* [27] proposed a diatomic mass-spring chain with embedded local resonators, stating that the topological interface states cannot exist in the local resonance band gap (LRBG) but can be supported in a Bragg scattering band gap (BSBG) in subwavelength frequencies. The topological characteristics of the uniform beam model with periodically attached local resonators were also investigated by different researchers [28–31], where the topological phase transition

could be achieved by altering the spacing between the two resonators in a unit cell. Although the 1D topological mechanical metamaterials have been extensively explored and developed in recent years, it is a widely held view that the topological phase transition mainly occurs in the BSBGs. The role of local resonance is merely utilized to lower the band frequency and achieve subwavelength topological states. To the best knowledge of the authors, in 1D mechanical systems, the topological states in the LRBGs are rarely reported. As in-gap states, the topological state receives the influence of the properties of the band gap in which it is located. The topological state within the LRBG is expected to exhibit stronger energy localization, which will significantly improve the application prospects for 1D topological metamaterials for energy harvesting.

Indeed, in recent years, the topological locally resonant edge states have been found and studied in higher dimensional 2D and 3D topological systems, which can provide valuable inspiration and guidance for 1D topological local resonance systems. In a two-dimensional slit-typed sonic crystal, Chen *et al* [32] observed topological locally resonant and Bragg edge modes and analyzed the two topological edge states based on different mechanisms. Zhang *et al* [33] reported Dirac degeneracies induced by the locally resonant states in a 2D phononic crystal plate and demonstrated the propagation behavior of the topological interface modes in LRBG. By constructing Dirac valley degeneracies based on Bragg scattering and local resonance, the local-resonant phononic crystal plates have been demonstrated to support dual-band topologically valley-protected edge transmission [34, 35]. Exploiting multimodal local resonance, 3D topological metamaterials were presented to enable low-frequency elastic wave control over multiple distinct frequency bands, and the modal-polarization waveguide was achieved [36, 37]. Inspired by the advances of higher-dimension topological metamaterials, the local resonance mechanism should play a more significant role in 1D topological systems, rather than merely being used to lower the topological band frequency.

Beyond conventional periodic metamaterials, topological metamaterials have been demonstrated to be an excellent candidate for dual functionality application of vibration attenuation and energy trapping [38, 39], due to the combination of band gap and topological characteristics. To suppress broadband vibrations in the low-frequency regime, the metamaterial beams with periodic spring connections to the ground (i.e. beam-foundation system) have been designed and studied [40–42], which can induce a quasi-static band gap (QSBG) starting from 0 Hz by the elastic foundation. The propagation characteristics of flexural waves in a periodic beam on elastic foundations were first studied by Yu *et al* [40], and the low-frequency broad band gap of the beam on elastic foundations was demonstrated. Sun *et al* [43] designed a novel tunable

piezoelectric metamaterial beam on a periodic elastic foundation and obtained the wider band gap region by coupling multiple band gaps. Lim *et al* [44, 45] achieved topological phase transitions by alternately changing the elastic foundation parameters and developed a new topological rainbow trapping approach for metamaterial beam-foundation systems. Hu *et al* [46] demonstrated that the interface state in the QSBG of the 1D beam-foundation system can be tuned to an arbitrarily low frequency through mass-spring models. Overall, metamaterial beam-foundation systems have revealed great potential in the field of low-frequency vibration control and topological energy trapping. However, the existing metamaterial beam-foundation system lacks the utilization of local resonance mechanism, which may induce new band gaps and topological characteristics.

In this study, a novel 1D metamaterial beam-resonator-foundation system is proposed by inserting resonators into the conventional elastic foundation. Its band gap mechanism and topological characteristics are studied to achieve ultra-low frequency vibration attenuation and enhanced topological energy trapping. The rest of the paper is organized as follows. In section 2, the proposed model and the investigation methods for band structure are illustrated. Subsequently, in section 3, the topologically different band gaps are obtained by leveraging the band folding mechanism. The topological inversion of Bragg scattering and local resonance band gaps are discovered and demonstrated by the mode inversion and Zak phase. The underlying physical mechanism of the rarely reported topological phase transition of LRBGs in 1D topological metamaterials is revealed. The numerical implementation of both topological Bragg and locally resonant interface states and the examination of the robustness of topological protection are conducted in section 4. Finally, the main findings and conclusions of this work are summarized in section 5.

2. Modeling of 1D metamaterial beam-resonator-foundation system

Different from the conventional 1D metamaterial beam-foundation system that just places the beam on the elastic foundation [40, 45], in this study, an innovative metamaterial beam-resonator-foundation system is proposed by inserting resonators into the elastic foundation. The introduction of local resonance allows for more abundant band gap and topological characteristics. The geometrical model of the proposed metamaterial beam-resonator-foundation system is illustrated in figure 1(a). The aluminum beams (dark color) are connected to the aluminum resonators (dark color) via rubber pillars (light color), and then the aluminum resonators are connected to an ideally rigid foundation via the same rubber pillars, forming the 1D metamaterial beam-resonator-foundation system.

The metamaterial system can be considered as a periodic replication of a unit cell along the x -axis, which is shown in the enlarged view in figure 1(a). In essence, the unit cell consists of

four minimal units, where the two units in the middle are considered as a group and the two units at the ends are regarded as another group, illustrated in orange and blue, respectively. The units in a group have the same structural parameters, thus ensuring the mirror symmetry of the structure regardless of parameter tuning. The dimensions of the element beam are unified as length a , width b , and thickness h , thus the lattice constant of the unit cell is $L = 4a$. The radii of the two groups of rubber pillars and resonators are denoted by r_1/r_2 and R_1/R_2 , and the heights of all rubber pillars and resonators are unified as h_1 and h_2 . The solid model can be simplified into the corresponding beam-mass-spring system, as shown in figure 1(b), where the two groups of rubber pillars and the aluminum resonators are equated into springs k_1/k_2 and local resonance masses m_1/m_2 , respectively.

In this study, in accordance with the simplified model (figure 1(b)) and the solid model (figure 1(a)), the band structures of the proposed structure are investigated theoretically and numerically with the transfer matrix method (TTM) and finite element method (FEM), respectively.

2.1. Transfer matrix method

Based on the simplified model (figure 1(b)) and the Euler-Bernoulli beam theory suitable for thin beam analysis, the governing equation is given by

$$EI \frac{d^4}{dx^4} w(x, t) - \rho A \omega^2 w(x, t) + f(x, t) = 0 \quad (1)$$

where E is Young's modulus, I is the area moment of inertia, ρ is mass density, A is the cross-sectional area, and ω is the angular frequency. $f(x, t)$ is the reaction forces of the spring acting on the beam. $w(x, t)$ is deflection along the z -axis, which can be expressed as

$$w(x, t) = W(x) e^{i\omega t} \quad (2)$$

where $W(x)$ is the vibration attitude.

The general solution of $W(x)$ in equation (1) can be expressed as

$$W(x) = A \cosh(\lambda x) + B \sinh(\lambda x) + C \cos(\lambda x) + D \sin(\lambda x) \quad (3)$$

where $\lambda^4 = \rho A \omega^2 / EI$. The force analysis at the point of attachment of the resonator is critical for the analysis of the transfer relationship, thus the point of attachment of the spring is assumed to be the origin of the x coordinate. As for the local resonator in the 1st unit of the n th unit cell, considering the equilibrium condition for all the forces in the z -axis including the inertial force, one obtains

$$f_{n,1}^1(t) + f_{n,1}^2(t) + m_1 \ddot{z}_{n,1}(t) = 0 \quad (4)$$

where $z_{n,1}(t) = Z_{n,1} e^{i\omega t}$ is the z -direction displacement of the resonator, $f_{n,1}^1(t)$ and $f_{n,1}^2(t)$ are the force from the upper and lower springs. The force $f_{n,1}^1(t)$ is given by

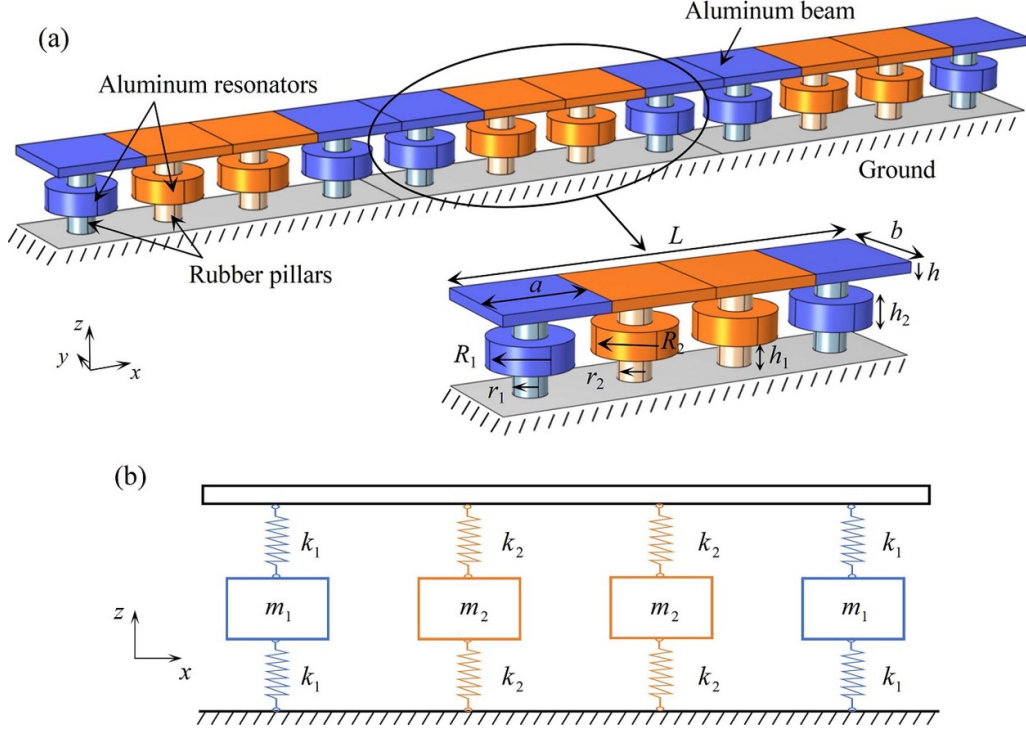


Figure 1. (a) Geometric illustration of the proposed metamaterial beam-resonator-foundation system and (b) the corresponding simplified beam-mass-spring model.

$$\begin{aligned} f_{n,1}^1(t) &= k_1 [z_{n,1}(t) - w(x_{n,1}, t)] \\ &= k_1 [Z_{n,1} - W_{n,1}(0)] e^{i\omega t} \triangleq F_{n,1}^1 e^{i\omega t}. \end{aligned} \quad (5)$$

where $\Psi_{n,1} = [A_n^1 \ B_n^1 \ C_n^1 \ D_n^1]^T$, $\Psi_{n-1,4} = [A_{n-1}^4 \ B_{n-1}^4 \ C_{n-1}^4 \ D_{n-1}^4]^T$,

The force $f_{n,1}^2(t)$ is given by

$$f_{n,1}^2(t) = k_1 [z_{n,1}(t)] = k_1 Z_{n,1} e^{i\omega t} \triangleq F_{n,1}^2 e^{i\omega t}. \quad (6)$$

Substituting equations (5) and (6) into equation (4) leads to

$$Z_{n,1} = \frac{k_1}{2k_1 - m_1 \omega^2} W_{n,1}(0). \quad (7)$$

The continuities of displacement, slope, bending moment, and shear force of the beam at the spring k_1 attachment point are formulated as

$$W_{n,1}(0) = W_{n-1,4}(a), \quad (8a)$$

$$W'_{n,1}(0) = W'_{n-1,4}(a), \quad (8b)$$

$$EIW''_{n,1}(0) = EIW''_{n-1,4}(a), \quad (8c)$$

$$EIW'''_{n,1}(0) - F_{n,1}^1 = EIW'''_{n-1,4}(a). \quad (8d)$$

Substituting equations (3) and (7) into equation (8), the 1st unit of the n th unit cell and the last (4th) unit of the $(n-1)$ th unit cell can be related as

$$\mathbf{K}_1 \Psi_{n,1} = \mathbf{H}_1 \Psi_{n-1,4} \quad (9)$$

$$\begin{aligned} \mathbf{H}_1 &= \begin{bmatrix} \cos(\lambda a) & \sin(\lambda a) & \cosh(\lambda a) & \sinh(\lambda a) \\ -\sin(\lambda a) & \cos(\lambda a) & \sinh(\lambda a) & \cosh(\lambda a) \\ -\cos(\lambda a) & -\sin(\lambda a) & \cosh(\lambda a) & \sinh(\lambda a) \\ \sin(\lambda a) & -\cos(\lambda a) & \sinh(\lambda a) & \cosh(\lambda a) \end{bmatrix} \\ \mathbf{K}_1 &= \begin{bmatrix} 1 & 0 & 1 & 0 \\ 0 & 1 & 0 & 1 \\ -1 & 0 & 1 & 0 \\ \frac{k_1^2 - k_1 m_1 \omega^2}{EI \lambda^3 (2k_1 - m_1 \omega^2)} & -1 & \frac{k_1^2 - k_1 m_1 \omega^2}{EI \lambda^3 (2k_1 - m_1 \omega^2)} & 1 \end{bmatrix} \end{aligned}$$

Similarly, the transfer matrix relation between the first (1st) unit and the second (2nd) unit of the n th unit cell can be derived based on the continuity conditions at the interface where the spring k_2 is attached

$$\mathbf{H}_2 \Psi_{n,1} = \mathbf{K}_2 \Psi_{n,2} \quad (10)$$

where $\Psi_{n,1} = [A_n^1 \ B_n^1 \ C_n^1 \ D_n^1]^T$, $\Psi_{n,2} = [A_n^2 \ B_n^2 \ C_n^2 \ D_n^2]^T$, $\mathbf{H}_2 = \mathbf{H}_1$,

$$\mathbf{K}_2 = \begin{bmatrix} 1 & 0 & 1 & 0 \\ 0 & 1 & 0 & 1 \\ -1 & 0 & 1 & 0 \\ \frac{k_2^2 - k_2 m_2 \omega^2}{EI \lambda^3 (2k_2 - m_2 \omega^2)} & -1 & \frac{k_2^2 - k_2 m_2 \omega^2}{EI \lambda^3 (2k_2 - m_2 \omega^2)} & 1 \end{bmatrix}.$$

Table 1. Geometric parameters of the metamaterial unit cell (mm).

L	a	b	h	h_1	h_2	R_1	R_2	r_1	r_2
160	40	40	4	10	10	15	15	6	6

Thus, the left and the right ends of a unit cell can be related by the transfer matrix \mathbf{T} :

$$\Psi_{n-1,4} = \underbrace{\mathbf{K}_1^{-1} \mathbf{H}_1 \mathbf{K}_2^{-1} \mathbf{H}_2 \mathbf{K}_2^{-1} \mathbf{H}_2 \mathbf{K}_1^{-1} \mathbf{H}_1}_{\mathbf{T}} \Psi_{n,4}. \quad (11)$$

According to the Bloch's theorem, the periodicity in the x -direction implies the below relation equation:

$$\Psi_n = e^{iq} \Psi_{n-1}. \quad (12)$$

A standard eigenvalue problem results from the mediation between equations (11) and (12):

$$|\mathbf{T} - e^{iq} \mathbf{I}| = 0 \quad (13)$$

where \mathbf{I} is a 4-by-4 identity matrix. The relationship between the angular frequency ω and the wave vector \mathbf{q} in the infinite periodic structure, i.e., the dispersion relation, can be obtained by solving the eigenvalues of the matrix \mathbf{T} .

2.2. Finite element analysis

In addition to the theoretical band analysis with the simplified mass-spring model, the FEM is employed to calculate the band structure of the solid model (figure 1(a)). A finite element analysis of the system proposed in this study is performed by using the FEM Package COMSOL Multiphysics 6.0. The solid mechanics module is utilized to derive the structure mode shapes and band structures via an eigenfrequency study. The Floquet periodicity condition is applied to the left and right boundaries of a unit cell. The fixed constraint boundary condition is applied to the bottom surface of the rubber pillars, which limits all the degrees of freedom of the bottom surface and thus simulates the connection between the spring and the ground. The Bloch vector \mathbf{q} is scanned from 0 to π/L to obtain the band structure, where L is the lattice constant. In the simulation, Young's modulus (E), density (ρ), and Poisson's ratio (ν) of the aluminum (rubber) are 70 GPa (50 MPa), 2700 kg m⁻³ (1000 kg m⁻³), and 0.33 (0.48). The specific geometric parameters are listed in table 1. The extra fine mesh size predefined in the physical field is leveraged to ensure accurate numerical results. Furthermore, it should be stated that the wave vector \mathbf{q} is normalized as 0–1 in all band structures of the following paper.

3. Band gap mechanism and topological analysis

3.1. Band structures

Band folding is a classical mechanism for achieving topological phase transitions in 1D systems [28, 47], which can be implemented by doubling unit cell. Therefore, at the beginning, the process of band folding together with the doubling

of unit cell is displayed to shed light on the underlying topological mechanism of the proposed model. As mentioned in the model description, the proposed unit cell is actually comprised of four minimal elementary units. In other words, the minimal unit cell consists of only one elementary unit. Figures 2(a) and (b) show the schematic diagram of the minimal unit cell doubling once and the minimal unit cell doubling twice. After doubling the minimal unit twice, the proposed unit cell is obtained. For theoretical analysis, the geometry parameters listed in table 1 are equated to the corresponding stiffness and mass parameters as $k = 623\,986 \text{ N m}^{-1}$, $m = \rho V = 0.0191 \text{ kg}$. The equivalent stiffness is obtained by calculating the force-displacement response through COMSOL (i.e. one end of the rubber pillar is fixed and the other end is applied with pressure), and this equivalent method will be used throughout the study. Figures 2(c) and (d) display the evolution of band structure and the occurrence of band folding during the two unit cell doubling processes, where the red dashed curves and the black solid curves denote the bands before and after the unit cell doubling, respectively, and the hollow dots represent the band folding points.

In figure 2(c), there are only two bands (red dashed curve) in the considered frequency range (0–2500 Hz) for the minimal unit cell. After doubling the minimal unit cell into a unit cell with two elementary units, the new resulting band structure (black curve) can be obtained by folding the previous bands along the crease $\mathbf{q} = 0.5$. The number of bands increases to four, and two band folding points are formed at the boundary of the Brillouin zone ($\mathbf{q} = 1$). Similarly, when the unit cell with two elementary units is doubled to a unit cell with four elementary units, the four bands before the doubling are folded along $\mathbf{q} = 0.5$ to form eight bands. It is worth noting that the two previous band folding points are mirrored to the center of the Brillouin zone ($\mathbf{q} = 0$) and three new band folding points appear at the boundary of the Brillouin zone. This means that there are five band folding points in the proposed model that can be opened by breaking spatial symmetry, and the topological properties of these band folding points will be investigated in detail below.

In accordance with the geometrical parameters listed in table 1, figure 3(a) shows the band structure of the default unit cell ($R_1 = R_2 = 15 \text{ mm}$, $r_1 = r_2 = 6 \text{ mm}$) obtained by the theoretical TMM and the FEM. In this study, the symmetric out-of-plane flexural wave of the beam is more concerned, and the bands corresponding to torsional modes and longitudinal modes are eliminated through mode analysis. There are some small frequency deviations between the results obtained by the two methods, which may be caused by the inability of the theoretical model to capture the slight torsion of the resonator and the neglect of rubber pillar mass. Nonetheless, the agreement between the results of the two methods is still sufficient to verify the correctness of our

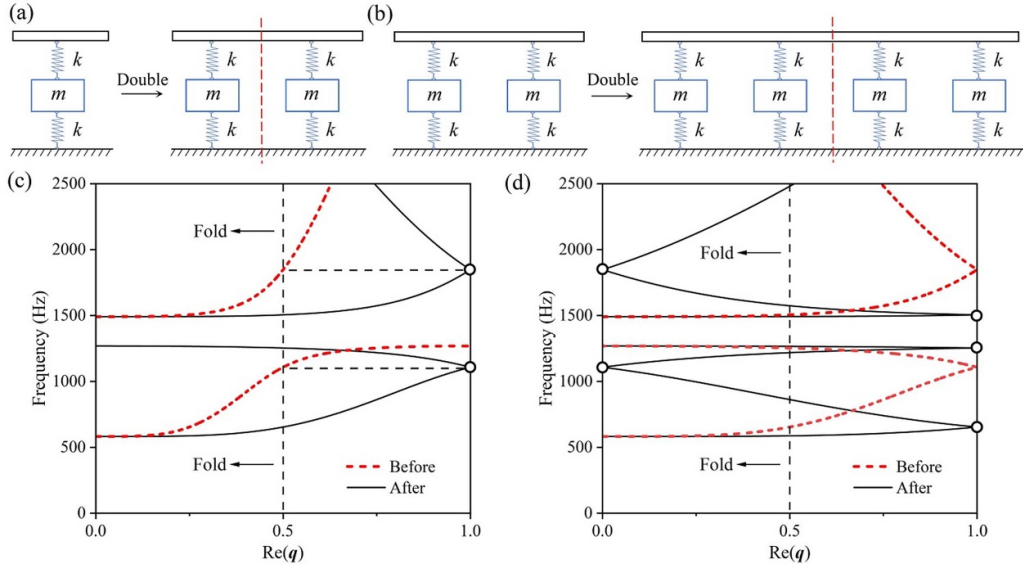


Figure 2. Schematics of (a) the minimal unit cell doubling once and (b) doubling twice. (c)–(d) Illustration of the band folding process, where the red dashed and black solid curves denote the band structures before and after the unit cell doubling, respectively, and the hollow dots denote the band folding points.

band structure theory and calculation method. For the default unit cell, a quasi-static band gap (QSBG) induced by the period elastic foundation appears at 0–614 Hz, and a LRBG forms at 1300–1564 Hz due to the introduction of resonators, which are marked with blue and yellow respectively. In essence, the QSBG is attributed to the connection of the spring to the ground, and the band gap width is proportional to the spring stiffness [40, 44, 45], which can be leveraged for ultra-low frequency vibration control. Different from the conventional beam-foundation system, the introduction of resonators allows us to design different resonance systems to obtain abundant band gap characteristics and novel topological states.

A significant amount of metamaterial research studies have shown that the imaginary part of wave vector \mathbf{q} can evaluate the attenuation capacity of the band gap and reflect the origin of the band gap, as the larger the imaginary part of wave vector \mathbf{q} , the stronger the attenuation capacity of the band gap [48, 49]. Thus, figure 3(b) shows the imaginary \mathbf{q} obtained by theoretical analysis. The imaginary part of wave vector \mathbf{q} in the QSBG is generally of small magnitude and varies smoothly, implying the Bragg scatter mechanism. While the imaginary part of wave vector \mathbf{q} in the LRBG is relatively large and exhibits asymmetric resonance peaks. The red dashed curve indicates the local resonance frequency of resonators, which is calculated by equation (14). There is good agreement between the attenuation peaks and the calculated resonance frequencies, verifying the local resonance mechanism of the band gap as well as the correctness of the theoretical analysis. Figure 3(c) further displays the modes of edges of the two band gaps. It can be observed that the mode at the edge of the QSBG is dominated by out-of-plane vibration of the beam, while the vibration is remarkably confined to the four resonators in the modes at the edges of the LRBG, demonstrating the different Bragg scattering and local resonance mechanism of the two band gaps.

$$f_{LR} = \frac{1}{2\pi} \sqrt{\frac{2k}{m}}. \quad (14)$$

Subsequently, the identical two groups of geometric parameters in a unit cell will be changed to different ones, and two mutually reciprocal unit cells I ($R_1 = 10$ mm, $R_2 = 15$ mm and $r_1 = 6$ mm, $r_2 = 5.4$ mm) and II ($R_1 = 15$ mm, $R_2 = 10$ mm and $r_1 = 5.4$ mm, $r_2 = 6$ mm) are constructed. The variation of the radii of the rubber pillars and resonators leads to changes in the stiffness and mass of the local resonance system. Thus, the equivalent stiffness and mass parameters for theoretical analysis are changed to $k_1/k_2 = 623\,986/500\,250$ N m⁻¹, $m_1/m_2 = 0.0191/0.0085$ kg. The unit cells I and II share an identical band structure, as shown in figure 3(d). All the five band folding points are opened to generate new band gaps, which are termed as band folding induced band gap and highlighted with white stripes. To distinguish the underlying mechanism of these band gaps, the corresponding imaginary part of wave vector \mathbf{q} is depicted in figure 3(e). It can be observed that two LRBGs appear due to the two different resonators, which are evidently related to the two resonance frequencies marked with red dashed curves in figure 3(e) and thus marked with yellow in figure 3(d). For ease of distinction, the two band gaps are termed LRBGs 1 and 2 in the order from low frequency to high frequency hereafter, as designated with boxed numbers (1, 2). Except for the QSBG marked with blue, there are also four BSBGs due to the small and symmetric imaginary \mathbf{q} , which are marked with red in figure 3(d). Similarly, these band gaps are named BSBGs 1–4 in the order from low frequency to high frequency hereafter and indicated with circled numbers (1, 2, 3, 4) in figure 3(d). It is notable that there are three BSBGs (1, 2, 4) and two LRBGs among the five newly generated band gaps induced by band folding, which are indicated with white stripes. The BSBG 3 seems to occupy the location of the previous LRBG of the default unit cell (between the 4th and 5th dispersion curves), implying that the nature of this

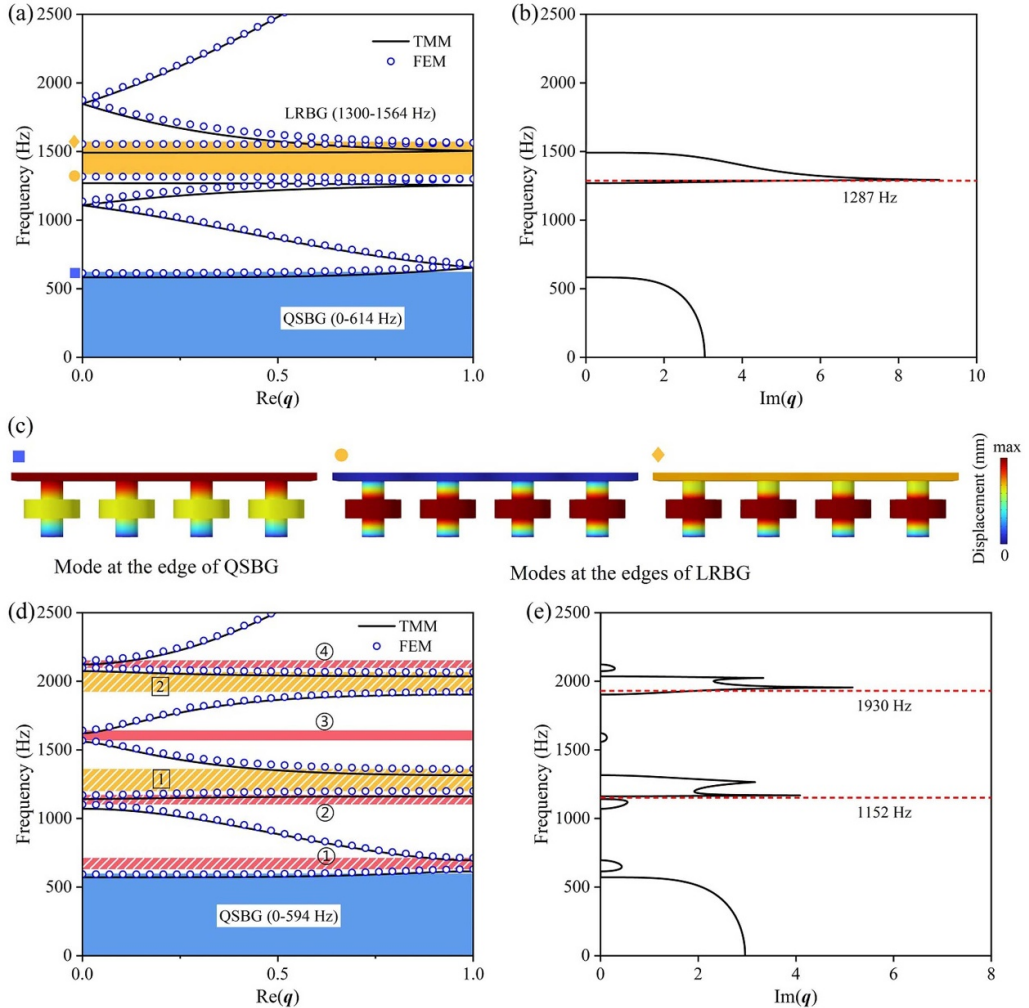


Figure 3. (a) Band structure of the default unit cell ($R_1 = R_2 = 15 \text{ mm}$, $r_1 = r_2 = 6 \text{ mm}$) obtained by the theoretical transfer matrix method (TMM) and the finite element method (FEM), and (b) the corresponding imaginary wave vector q . (c) Modes at the edges of the quasi-static band gap and local resonance band gap. (d) Band structure of the unit cell I ($R_1 = 10 \text{ mm}$, $R_2 = 15 \text{ mm}$ and $r_1 = 6 \text{ mm}$, $r_2 = 5.4 \text{ mm}$) and unit cell II ($R_1 = 15 \text{ mm}$, $R_2 = 10 \text{ mm}$ and $r_1 = 5.4 \text{ mm}$, $r_2 = 6 \text{ mm}$) obtained by the TMM and FEM, and (e) the corresponding imaginary wave vector q .

band gap transitions from local resonance to Bragg scattering with parameter variation.

In fact, the nature of the band gap is not immutable, and band gaps based on different mechanisms can be coupled and transitioned, which has been investigated and demonstrated in some metamaterial research [50–53]. To illustrate the transition of band gap nature in our model, the variation of the three band gaps (the initial LRBG in default unit cell and the two band folding induced band gaps above and below this band gap) with parameters change are investigated. Keeping all other parameters of the default unit cell constant, the radius of resonator R_1 is gradually reduced. Figures 4(a) and (b) show the variation of band structure and the corresponding imaginary wavevector with respect to R_1 , respectively. It can be observed that when the change of R_1 is tiny ($R_1 = 14.5 \text{ mm}$), the opened two band folding induced band gaps are BSBGs, consistent with the common 1D topological systems. However, with further

changes to R_1 , the imaginary wavevector of the two band folding induced band gaps gradually increases and appears resonance peaks, which eventually evolve into LRBGs. In contrast, the imaginary wavevector of the initial LRBG decreases and becomes smooth with the decrease of R_1 . In cases 3 and 4 ($R_1 = 14/13 \text{ mm}$), it is difficult to determine whether the three band gaps are LRBG or BSBG. These band gaps can be regarded as the intermediate states in the transition of band gap nature and are marked with the gradient colors between yellow and red. The results clearly explain why the two opened band-folding band gaps in figure 3(d) are locally resonant and how a single LRBG in figure 3(a) evolves into two. More importantly, it is revealed that band folding induced band gaps can undergo the band gap transition from Bragg to local resonance, laying the foundation for achieving topologically local resonance band gaps.

After demonstrating the transition of the band gap nature, a more detailed parametric analysis is conducted to gain a

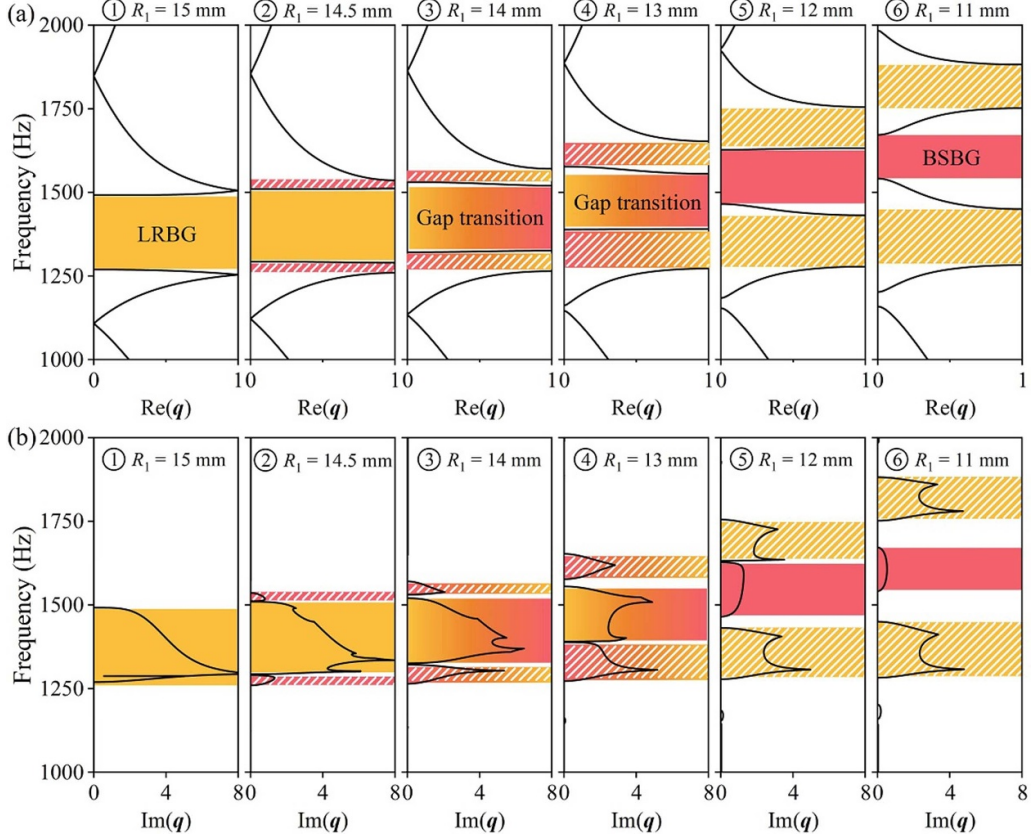


Figure 4. (a) The band structure variation with respect to the radius of resonator R_1 . (b) The imaginary wavevector q corresponding to specific parameters in (a). The yellow and red represent LRBG and BSBG, the white stripes denoted band folding induced band gap. The gradient colors between yellow and red are used to indicate band gap transition.

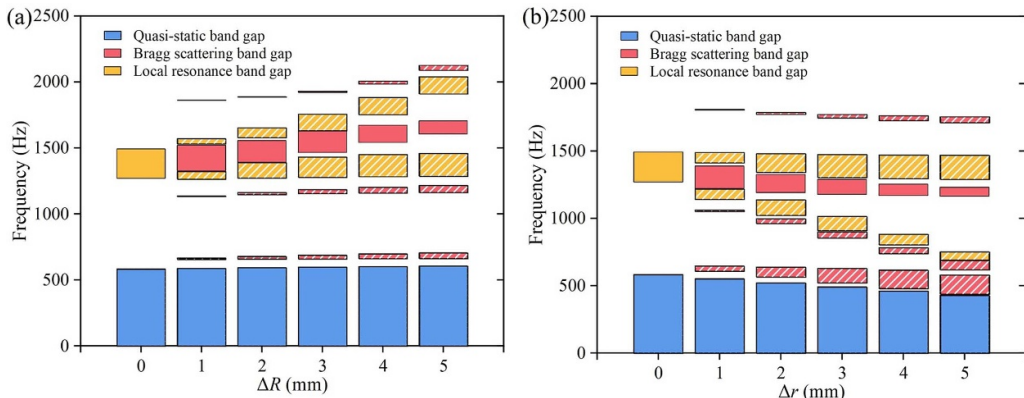


Figure 5. The variation of band gap range with respect to (a) the decrement ΔR of the radius of the resonator R_1 and (b) the decrement Δr of the radius of the rubber pillar r_1 . Different colors indicate band gaps with different mechanisms and the white stripes denote the five newly generated band gaps induced by band folding.

better insight into the evolution of all band gaps. Using the parameters in table 1 as a reference, the radius of the resonator R_2 remains constant while the radius R_1 undergoes gradual reduction. Figure 5(a) shows the variation of band gap range with respect to the decrement ΔR of the radius of the resonator R_1 . The colors and stripes of band gaps have the same meaning as those in figures 3(a) and (d). It can be observed that with the variation of ΔR , a single LRBG is divided into

two separate LRBGs, which arises from the different local resonance frequencies of the resonators. The LRBG in the default unit cell transforms into a narrow BSBG gradually. With the increase of ΔR , the symmetry of the structure is further broken, and thus the five band folding induced band gaps are wider. Furthermore, the decrease of R_1 implies the increase of the local resonance frequency, so that all band gaps exhibit a tendency to move towards higher frequencies.

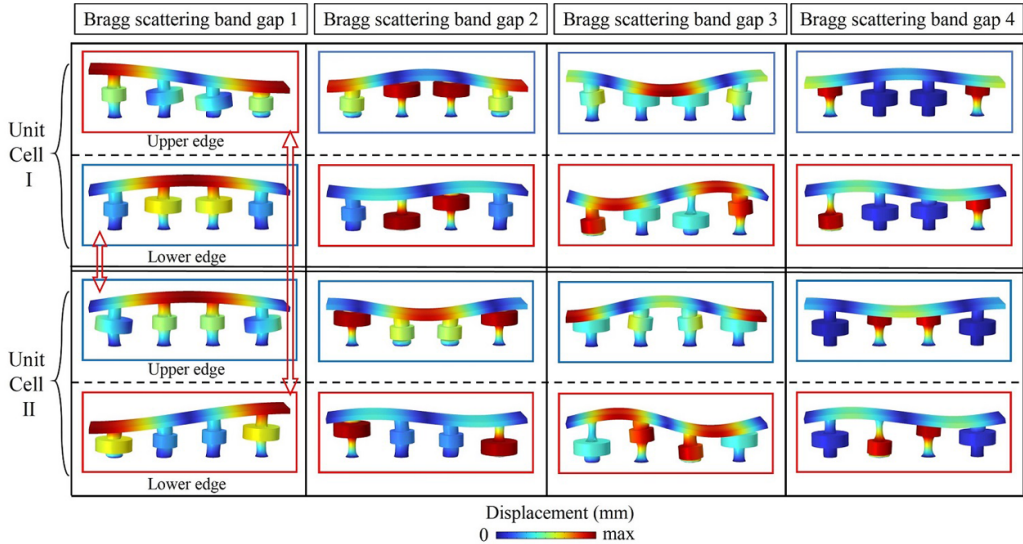


Figure 6. Modes at the edges of the four Bragg scattering band gaps for the two unit cells I and II. The blue and red boxes denote the even and odd modes, respectively.

The variation of band gap range with respect to the change of the rubber pillar radius r_1 is also investigated. Similarly, while keeping the radius of the rubber pillar r_2 unchanged, r_1 is gradually reduced. As shown in figure 5(b), the BSBG 1 can be significantly broadened with the decline of the rubber pillar radius. Moreover, compared with the resonator radius, the QSBG is more susceptible to the influence of rubber radius, since the stiffer the rubber pillar, the wider the QSBG [40, 44]. All band gaps tend to move towards lower frequencies with the decrease of r_1 , due to the decrease of the local resonance frequency. A sufficient band gap width is not only beneficial for vibration attenuation but also conducive to inducing the topological states. Therefore, simultaneous modulation of resonator mass and spring stiffness is a more efficient method to achieve broad band gaps and topological states.

3.2. Mode inversion and Zak phase transition

In the previous subsection, all five band folding points are opened by breaking spatial symmetry, and the topological properties of these band gaps will be examined in this subsection. The mode inversion between the upper and lower boundaries of band gaps is the most direct evidence of topological phase transition. Therefore, modes at the edges of four BSBGs 1–4 of unit cells I and II are shown in figure 6. The mode inversion occurs between the upper and lower edges of the BSBG 1 of the two types of unit cells, but it does not appear at other edges of BSBGs. Specifically, modes can be divided into even modes and odd modes according to whether they are symmetric about the central axis or not, which are denoted by the blue and red boxes in figure 6. The mode at the upper

edge of topological band gap 1 in the unit cell I is antisymmetric odd mode, which is similar to the mode at the lower edge of topological band gap 1 in the unit cell II. Meanwhile, the mode at the lower edge of BSBG 1 in the unit cell I is similar to the mode at the upper edge of BSBG 1 in the unit cell II. Therefore, the mode inversion implies that only BSBG 1 can be topologically different for the two unit cells, not all four Bragg band gaps. Reviewing the process of band gap formation (figures 3(a) and (d)), the BSBG 3 is degenerated by the LRBG of the default unit cell, not induced by the band folding, so it has no theoretical possibility of supporting topological inversion. For BSBGs 2 and 4, although they are band gaps induced by band folding, the band folding point is at the center of the Brillouin zone rather than the boundary, which may lead to the disappearance of the topological properties of these band folding points.

However, the mode inversion appears at the edges of the two LRBGs, as shown in figure 7, which has been rarely reported in 1D topological mechanical systems. The apparent mode inversion between the upper and lower band gap edges of the two unit cells implies that the two LRBGs for the two unit cells can also be topologically different, which can induce topological locally resonant interface states. As a result, recalling the five band folding points in figure 3(a), the mode results here manifest that the two band folding points at the center of the Brillouin zone do not appear to support the topological phase transition. Only the band gaps opened by lifting the three band folding points at the boundary of the Brillouin zone demonstrate the mode inversion.

To further determine the topological properties of band gaps, the topological invariant in the 1D system i.e. Zak phase is leveraged to capture the topological feature of dispersion

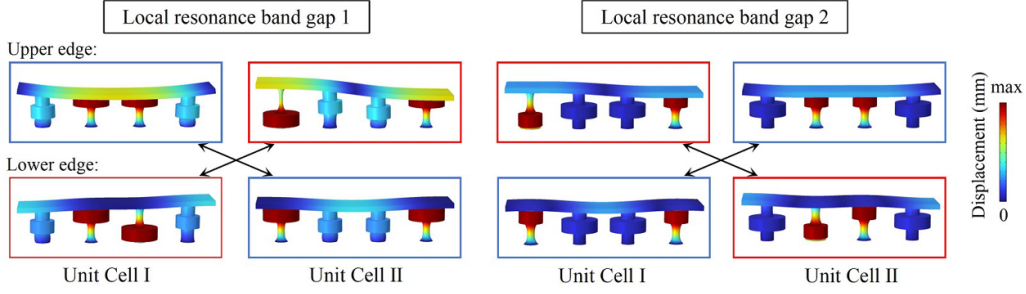


Figure 7. Modes at the edges of the two local resonance band gaps. The red and blue boxes denote the odd and even modes, respectively.

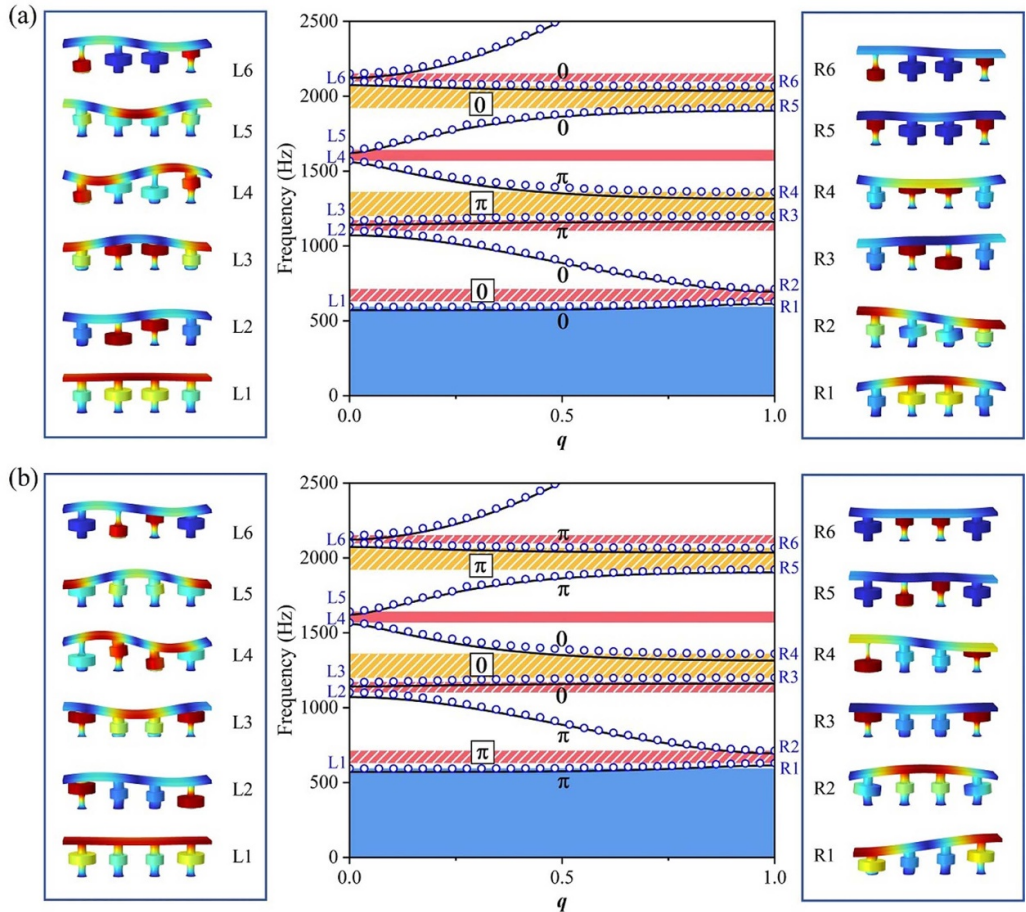


Figure 8. Zak phase identification for dispersion curves of the unit cell (a) I and (b) II. The Zak phase of each band is marked at the center of the band.

curves of the two unit cells [54, 55], which can be calculated as follows:

$$\theta_n^{\text{Zak}} = i \oint dq \int_{\Omega} \left(u^* \frac{\partial}{\partial q} u \right) dv \quad (15)$$

where n represents the n th pass band, u is the periodic in-cell displacement with $u = e^{-iq}w$, w is the normal mode function and the superscript * denotes a complex conjugation.

Due to the space symmetry of the structure, the Zak phase can only take 0 or π . The Zak phase can also be deferred by comparing the mode symmetries of the band at the cen-

ter and boundary of the Brillouin zone [16], which is a more simple and effective method. Figures 8(a) and (b) demonstrate the Zak phase identification for the unit cell I and II, respectively. The panels at the two sides of the band structure are modes at the center and boundary of the Brillouin zone respectively. If the modes at the center and boundary of the Brillouin zone of a band have the same symmetry, that is, both are even modes or odd modes in the meanwhile, the Zak phase of the band should be 0. On the contrary, when the symmetries of the modes in the center and boundary of the Brillouin zone of a band are opposite, the Zak phase of the band is π .

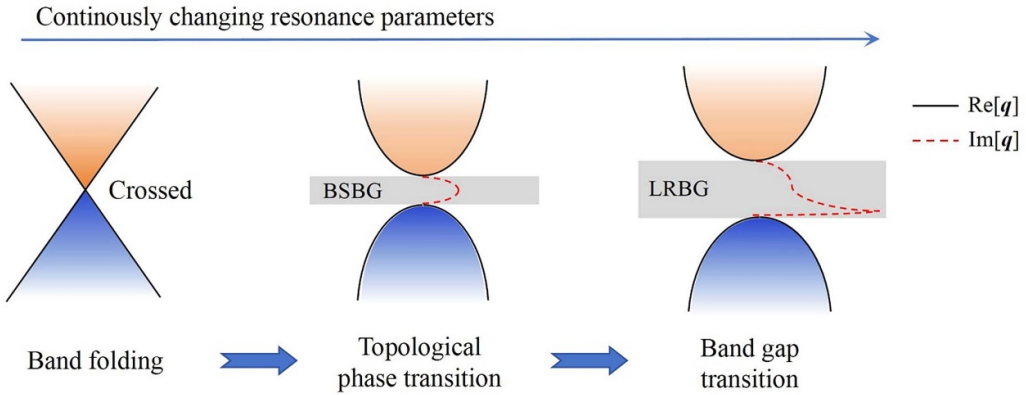


Figure 9. The underlying physical mechanism for the topological phase transition of local resonance band gap.

The topological properties of the band gap can be determined by summing the Zak phase of the dispersion curves below the band gap, i.e. $\vartheta_n = \sum_n^1 \theta_n^{\text{Zak}} \text{Mod} 2\pi$. It can be derived readily that the BSBG 1, and the LRBGs 1 and 2 for the unit cells I and II have different topological indexes 0 and π . The topological indexes of the rest band gaps are identical for the two unit cells. The conflict of the Zak phase provides a deep insight into the topological phase transition from the perspective of topological theory. These facts further validate that there are three topologically distinct band gaps for the two unit cells I and II. Therefore, according to the bulk-edge corresponding relationship [27], three topological interface states are expected to appear at the interface constructed with two topologically different unit cells.

Besides, it is necessary to give a further physical explanation for the rare topological phase transition of the LRBG in 1D topological metamaterials. Figure 9 reveals the underlying formation principle for the topological LRBG by summarizing the foregoing topological properties and band gap evolution studies. In our study, topological phase transitions are demonstrated to be induced by opening the band folding points at the boundary of the Brillouin zone. Recalling the band evolution process in figure 4, the topological band gaps induced by band folding undergo transitions in the nature of band gap from Bragg scattering to local resonance, with small to drastic changes in the resonance parameters. Although the nature of the band gap has changed, the topological characteristics guaranteed by the band folding points persist, which finally induces the topological inversion in LRBGs. In other words, a conventional topological Bragg band gap is promising to transform into a topological LRBG through a band gap transition. This approach to achieving the topological phase transition of LRBG is expected to be extended to similar local resonance systems, and related research is being developed (see a very recent preprint on arXiv [56]).

As in-gap states, the topological state receives the influence of the properties of the band gap in which it is located. In most existing studies of 1D topological systems, the role of local resonance is merely to lower the band frequency and

achieve subwavelength topological states [27, 28]. The topological states still are supported by BSBG. Thus, the topological Bragg interface states exhibit weaker vibration attenuation and energy localization capacities due to the Bragg scattering mechanism. However, the topological interface state in LRBG is expected to exhibit stronger energy localization properties than the conventional topological interface state in BSBG, which will be illustrated in the subsequent study.

3.3. Supercell analysis

To further demonstrate the existence of topological interface states in the three topologically different band gaps, a supercell is constructed by 3 cells of unit cell I and 3 cells of unit cell II. The Bloch periodic boundary conditions are applied to the left and right ends of the supercell to calculate the band structure. Figure 10(a) presents the band structure of the supercell. There are two flat bands that imply strong energy-localized modes in the topological band gap 1, and two nearly overlapped flat bands also appear in each of the two LRBGs. The modes corresponding to these flat bands at $q = 0.5$ are plotted in figure 10(b). It can be seen that the two flat bands in one band gap correspond to the topological interface state and topological boundary state respectively, where the energy is highly concentrated at the interface and boundary of the supercell. More interestingly, the topological states originated from the BSBG and the LRBG are obviously distinct. For the topological states in the BSBG 1, most of the energy is confined to the beam near the supercell interface rather than the resonators. Whereas, for the topological states in the LRBGs, the energy can be extremely strongly trapped by the resonators, which is quite different from the traditional topological states in the previous literature. On the other hand, the topological states in LRBGs can significantly reduce the vibration of the host structure under the topological state, which offers a superior avenue for achieving the dual functionality of vibration attenuation and energy trapping within the same structure.

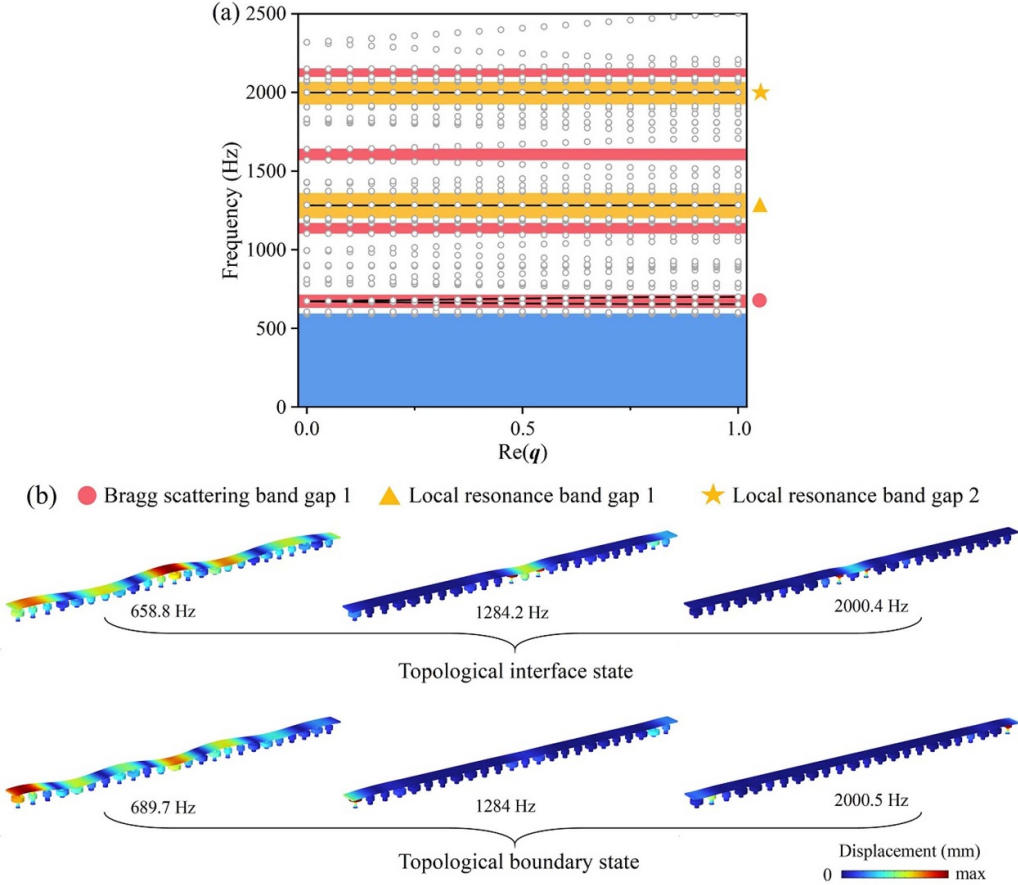


Figure 10. (a) Band structure of the supercell consisting of 3 cells of unit cell I and 3 cells of unit cell II. (b) The modes of the flat bands at $q = 0.5$, which are categorized into two types: topological interface state and topological boundary state.

4. Implementation and examination of topological interface states

4.1. Numerical implementation

After determining the topological properties of the band gaps and demonstrating the existence of topological interface states, the implementation of topological interface states as well as the examination of topologically protected robustness will be conducted in this section.

Figure 11(a) displays the schematic diagram for the transmission characteristics examination of the finite unit cell system consisting of 3 unit cells I and 3 unit cells II. A z -direction point harmonic excitation with an amplitude of 1 mm is applied to the left end of the system. To examine the vibration transmission characteristics of the metamaterial, the transmittance is defined as

$$\eta = 20\log_{10} \left| \frac{U_1}{U_0} \right| \quad (16)$$

where U_0 and U_1 denote the displacement amplitudes of the excitation point and response point, respectively.

In order to demonstrate the topological interface state more intuitively, the vibration response is extracted from the system interface and the right side at the same time. Transmittance

curves obtained through numerical simulation are illustrated in figure 11(b), with the colors and frequency ranges of band gaps matching those depicted in the band structure of figure 3(d). In accordance with the definition of transmittance in equation (16), a transmittance less than 0 implies that wave propagation is inhibited, while a transmittance greater than 0 indicates that waves can propagate freely. The boundary transmittance curve indicates that wave propagation can be well suppressed within the band gap range since the transmittance is less than 0 within the band gaps. In particular, the BSBGs 1–4 marked with red present weaker vibration attenuation abilities, validating the prediction of the band gap vibration reduction capacity derived from the imaginary wave vector. More importantly, from the interface transmittance curve, it is evident that a transmission peak denoted by the blue star emerges within each of the three topologically distinct band gaps, which is attributed to the presence of topological interface states. Meanwhile, it should be mentioned that the transmittance peaks in other band gaps are caused by torsional and translational resonances and do not belong to any topological states, which can be illustrated more clearly by comparing the transmission characteristics of the finite system without the interface shown in figure A1 in the appendix.

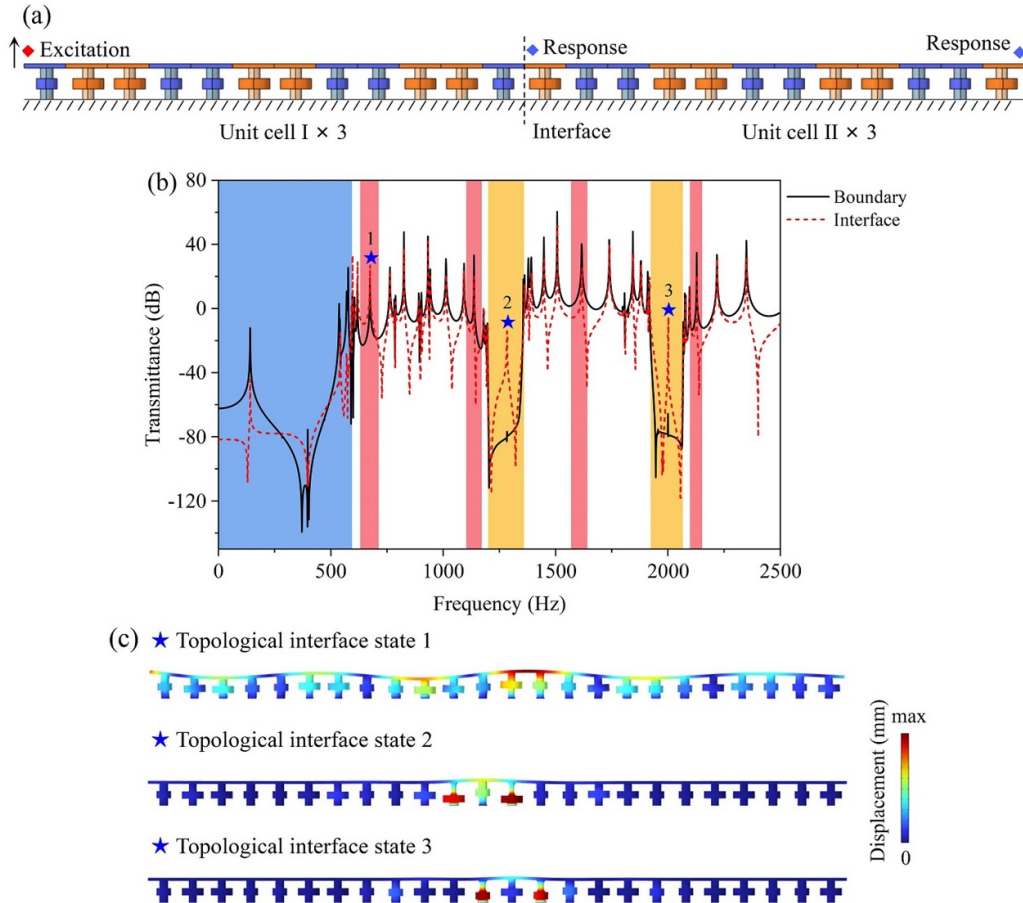


Figure 11. (a) Schematic for the transmission characteristics examination of the metamaterial system with finite unit cells. (b) The transmittance curves obtained by numerical simulation. (c) Simulated displacement fields for the three topological interface states.

Under the three marked transmittance peak frequencies, the simulated displacement fields for the three topological interface states are depicted in figure 11(c). As expected, the vibration energy can be highly concentrated in the vicinity of the interface at topological interface states. However, the displacement fields of the three topological interface states are quite different. Specifically, more energy is distributed over the beam rather than the resonators in the displacement field of the topological interface state 1 for the underlying Bragg mechanism of the band gap. At the topological locally resonant interface states 2 and 3 in the two LRBGs, the vibration energy is remarkably concentrated on the larger and smaller resonators near the interface respectively, and only a small amount of energy is distributed on the beam near the interface. Besides, the wave localization capacity of the local resonance mechanism is so strong that very little energy can be transferred to the right side in this topological state, which accounts for the extremely large difference in the boundary and interface transmittance at the two topological interface states 2 and 3 in figure 11(a).

Compared to the conventional topological Bragg interface state 1, the topological locally resonant states in LRBGs can localize wave energy to fewer unit cells (even one unit cell) near the interface. The degree of energy localization can be quantified by dividing the elastic strain energy density of

the volume of the particular unit cells by that of the entire structure. Under the three topological interface states 1–3, the energy concentrated at the unit cell across the interface (half unit cell I and half unit II) can reach 40%, 97%, and 96%, respectively. Obviously, the topological interface states of LRBGs exhibit stronger local performance, which is more conducive to topological energy harvesting. It should be highlighted that although there are similar phenomena that the energy concentrated at the resonators in existing 1D topological local resonance systems, these topological states still appear at the BSBGs and can not exhibit such a strong concentration of energy.

In addition, figure 12 shows several typical simulated displacement fields inside and outside band gaps to further reveal the different band gap mechanisms. When the vibration frequency is outside band gaps, the vibration can propagate without attenuation throughout the system. However, within the QSBG and LRBGs, the vibration propagation is completely suppressed after passing through 1–2 unit cells. In the BSBG 1, more unit cells are required to attenuate the vibration, which also indicates the lower attenuation capability of the BSBG. Besides, in the LRBGs 1 and 2, the propagation of vibration can be quickly suppressed due to the resonance of the larger and smaller resonators respectively.

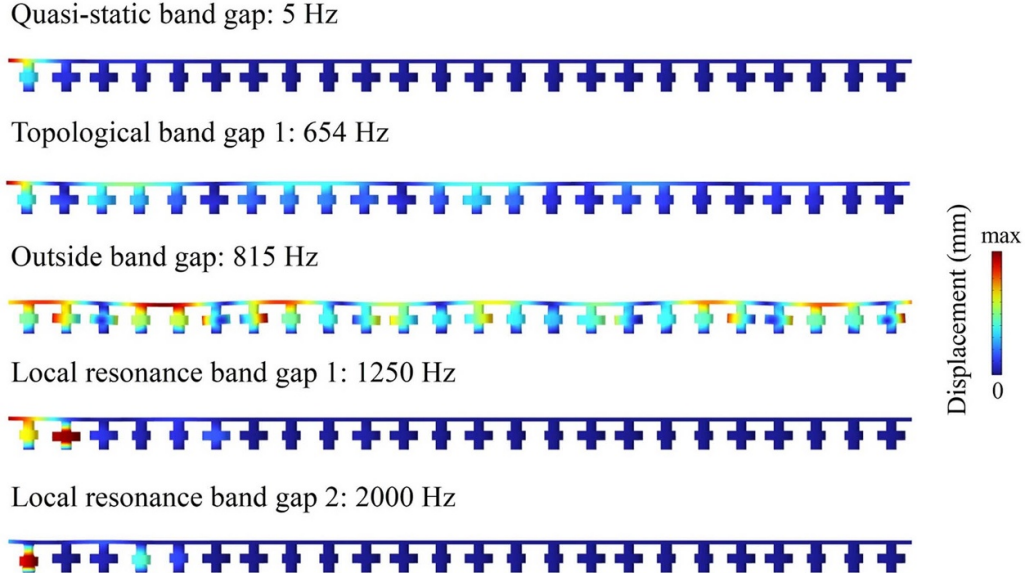


Figure 12. Simulated displacement fields inside and outside band gaps.

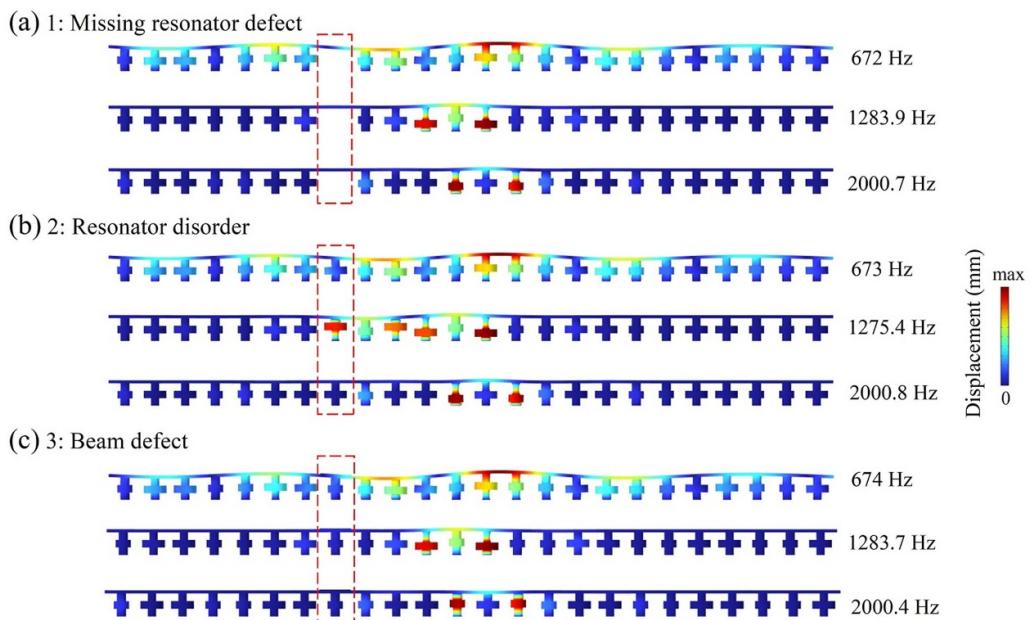


Figure 13. The robustness examination of topologically protected interface states under different defects and disorders. The simulated displacement field of the topological interface states with (a) missing a resonator in the second unit cell, (b) replacing a small resonator in the second unit cell with a larger one, and (c) raising the thickness of the beam in the second unit cell to 5 mm. The defective regions are labeled by the red dashed frames.

4.2. Robustness examination

As one of the most distinctive features of topological states, the topologically protected robustness guarantees that the topological state is immune to defects and disorders that occur during the construction and utilization process of the structure. Therefore, the robustness of topologically protected interface states is examined under three different defects and disorders, as shown in figure 13. The three defective structures arise from three different operations: missing a resonator in the second unit cell, replacing a small resonator in the second

unit cell with a larger one, and raising the thickness of the beam in the second unit cell to 5 mm, which are highlighted with red dashed frames. It can be seen that the topological interface states still maintain the expected displacement distribution of the energy concentration at the interface, apart from a slight shift in the excitation frequency of the interface states. Overall, all three types of topological interface states demonstrate excellent topological robustness against defects and disorders, laying a solid theoretical foundation for designing a stable energy harvesting system. The proposed metamaterial beam-resonator-foundation system

can be an excellent candidate for achieving ultra-low frequency vibration attenuation and enhanced topological energy trapping.

5. Conclusions

In this study, an innovative 1D metamaterial beam-resonator-foundation system is proposed by inserting resonators into the conventional elastic foundation. The band gap mechanism and topological characteristics of the proposed system are studied. The main findings are summarized as follows:

The introduction of local resonance allows for richer band gap characteristics compared to the existing beam-foundation metamaterial systems. In addition to a QSBG starting from 0 Hz due to the elastic foundation, a new LRBG is generated originating from local resonators. By folding the minimal unit cell twice, five band folding points can be obtained in the band structure. Subsequently, by adjusting the inner and outer resonance parameters, all the bandgap folding points can be opened and five band folding induced band gaps can be obtained. One LRBG evolves into two due to the two different types of resonators.

The topological properties of these band gaps are investigated thoroughly by the mode inversion and Zak phase. The band gaps obtained by lifting two band folding points at the center of the Brillouin zone do not support the topological phase transition. However, the topological phase transition occurs in the band gaps induced by the three band folding points at the boundary of the Brillouin zone, corresponding to one BSBG and two LRBGs. This study presents a novel observation of topological inversion in LRBGs of a 1D mechanical system. The underlying physical mechanism stems from the transition of band gap nature, that is, the topological inversion band gap transition from an initial BSBG to a LRBG with resonance parameters changes. The topological interface states are demonstrated to appear at the interface constructed by two topologically different unit cells. There are three different topological interface states, where the energy is localized at the beam and resonators near the interface, following the Bragg scattering and local resonance mechanism of band gaps in which the topological state is located. Compared to the conventional topological interface state in BSBG, the topological locally resonant interface state in LRBG can localize wave energy to fewer unit cells (even one unit cell) near the interface, exhibiting outstanding energy localization capacity. The robustness of topologically protected interface states is

validated by introducing defects and disorders into the perfect structure. Based on the demonstrated robust energy trapping, the proposed metamaterial beam-resonator-foundation system can be an excellent candidate for achieving topological energy harvesting.

Overall, this study can not only provide new insights into the topological theory of mechanical systems but also offer valuable inspiration for developing multi-functional devices integrating vibration attenuation and energy trapping.

Data availability statement

All data that support the findings of this study are included within the article (and any supplementary files).

Acknowledgment

The authors would like to acknowledge the financial support from the National Natural Science Foundation of China (12172383), the National Key R&D Program of China (2022YFB3806101-2), the Science and Technology Innovation Program of Hunan Province (2023RC3036, 2023JJ30644), and the Scholarship of China Scholarship Council (202306370135). We are grateful for resources from the High Performance Computing Center of Central South University.

Appendix

Figures A1(a) and (b) show the schematic for the transmission characteristics examination of the metamaterial system with finite unit cells consisting of 6 unit cells II and the corresponding transmittance curves, respectively. The finite unit cells system does not contain a topological interface and thus cannot support topological interface states. The excitation and response points are the same with figure 10. It can be observed that the transmittance peaks corresponding to topological interface states disappear in the three topological band gaps, while the transmittance peaks induced by torsional and translational resonances still exist in other band gaps. These results provide strong evidence for the topological origin of the transmission peaks corresponding to the topological interface states in figure 10.

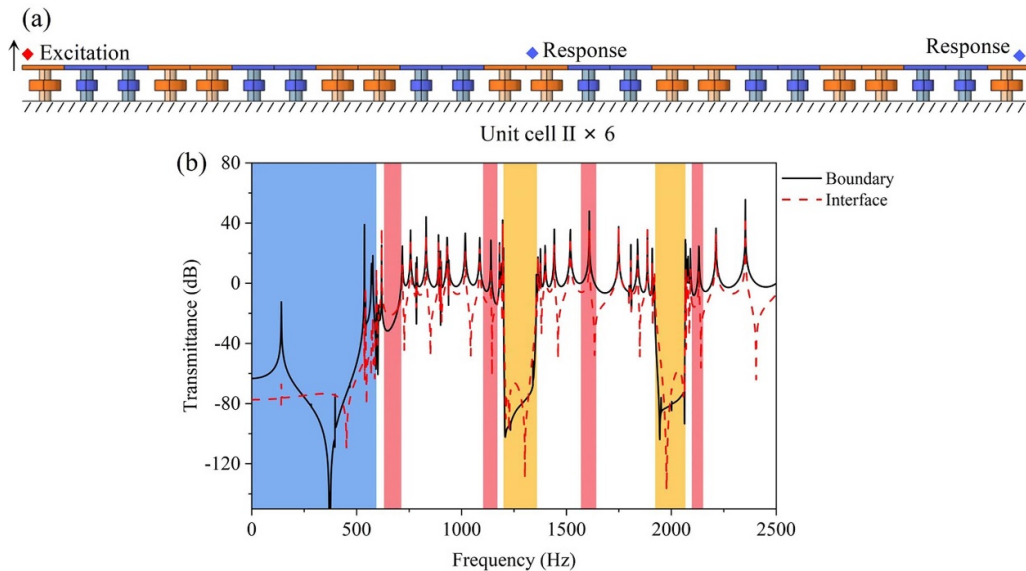


Figure A1. (a) Schematic for the transmission characteristics examination of the metamaterial system consisting of 6 unit cells II, and (b) the corresponding transmittance curves.

ORCID iDs

Hanqing Zhang <https://orcid.org/0000-0002-2807-8817>
 Lihua Tang <https://orcid.org/0000-0001-9031-4190>
 Guobiao Hu <https://orcid.org/0000-0002-1288-7564>
 Yingli Li <https://orcid.org/0000-0002-5843-2848>

References

- [1] Surjadi J U, Gao L, Du H, Li X, Xiong X, Fang N X and Lu Y 2019 Mechanical metamaterials and their engineering applications *Adv. Eng. Mater.* **21** 1800864
- [2] Dai H, Zhang X, Zheng Y, Pei W, Zhou R, Liu R and Gong Y 2022 Review and prospects of metamaterials used to control elastic waves and vibrations *Front. Phys.* **10** 1069454
- [3] Liu J, Guo H and Wang T 2020 A review of acoustic metamaterials and crystals *Crystals* **10** 305
- [4] Lin Q, Zhou J, Wang K, Xu D, Wen G and Wang Q 2023 Three-dimensional quasi-zero-stiffness metamaterial for low-frequency and wide complete band gap *Compos. Struct.* **307** 116656
- [5] Zhao P, Zhang K, Qi L and Deng Z 2022 3D chiral mechanical metamaterial for tailored band gap and manipulation of vibration isolation *Mech. Syst. Signal Process.* **180** 109430
- [6] Jiang W, Yin G, Xie L and Yin M 2022 Multifunctional 3D lattice metamaterials for vibration mitigation and energy absorption *Int. J. Mech. Sci.* **233** 107678
- [7] Huang H, Chen J and Huo S 2021 Recent advances in topological elastic metamaterials *J. Phys.: Condens. Matter* **33** 503002
- [8] Hong F, Zhang K, Qi L, Ding B and Deng Z 2023 High-frequency topological corner and edge states in elastic honeycomb plates *Int. J. Mech. Sci.* **246** 108141
- [9] Ni A and Shi Z 2024 Robust elastic shear wave transport in membrane-type topological metamaterials induced by material difference *Thin-Walled Struct.* **197** 111609
- [10] Zhang K, Hong F, Luo J and Deng Z 2021 Topological insulator in a hexagonal plate with droplet holes *J. Appl. Phys.* **54** 105502
- [11] Pirie H, Sadhuka S, Wang J, Andrei R and Hoffman J E 2022 Topological phononic logic *Phys. Rev. Lett.* **128** 15501
- [12] Dai H, Xue P, Lu E, Wang L and Zhou L 2023 Experimental realization of a soft topological acoustic switch *Phys. Rev. B* **107** 144105
- [13] Lee G, Lee S J, Rho J and Kim M 2023 Acoustic and mechanical metamaterials for energy harvesting and self-powered sensing applications *Mater. Today Energy* **37** 101387
- [14] Hu G, Tang L, Liang J, Lan C and Das R 2021 Acoustic-elastic metamaterials and phononic crystals for energy harvesting: a review *Smart Mater. Struct.* **30** 085025
- [15] Dai H, Xia B and Yu D 2021 Microparticles separation using acoustic topological insulators *Appl. Phys. Lett.* **119** 111601
- [16] Zhang H, Liu B, Zhang X, Wu Q and Wang X 2019 Zone folding induced tunable topological interface states in one-dimensional phononic crystal plates *Phys. Lett. A* **383** 2797–801
- [17] Huang H, Chen J and Huo S 2017 Simultaneous topological Bragg and locally resonant edge modes of shear horizontal guided wave in one-dimensional structure *J. Phys. D: Appl. Phys.* **50** 275102
- [18] Yu D, Hu G, Guo Z, Hong J and Yang Y 2023 Topological interface state formation in an hourglass lattice sandwich meta-structure *Int. J. Mech. Sci.* **246** 108170
- [19] Su W P, Schrieffer J R and Heeger A J 1979 Solitons in polyacetylene *Phys. Rev. Lett.* **42** 1698–701
- [20] Yin J, Ruzzene M, Wen J, Yu D, Cai L and Yue L 2018 Band transition and topological interface modes in 1D elastic phononic crystals *Sci. Rep.* **8** 6806
- [21] Huang Y, Huang Y, Chen W and Bao R 2020 Flexible manipulation of topologically protected waves in one-dimensional soft periodic plates *Int. J. Mech. Sci.* **170** 105348
- [22] Muhammad Z W and Lim C W 2019 Topological edge modeling and localization of protected interface modes in 1D phononic crystals for longitudinal and bending elastic waves *Int. J. Mech. Sci.* **159** 359–72
- [23] Park S and Jeon W 2023 Topological interface states in deep-subwavelength phononic beams *Mech. Syst. Signal Process.* **197** 110369
- [24] Chen Z, Wang G, Shi F and Lim C W 2022 Analytical modeling and numerical analysis for tunable topological

- phase transition of flexural waves in active sandwiched phononic beam systems *Int. J. Mech. Sci.* **223** 107292
- [25] Liu Y, Wang H, Fang W, Han Q, Liu D and Liang Y 2021 Tunable control of subwavelength topological interface modes in locally resonance piezoelectric metamaterials *Compos. Struct.* **276** 114541
- [26] Wu Z, Xia R, Yi J and Li Z 2023 Multiple topological interface modes in electromechanically resonant piezoelectric beams *Eng. Struct.* **281** 115716
- [27] Zhao D, Xiao M, Ling C W, Chan C T and Fung K H 2018 Topological interface modes in local resonant acoustic systems *Phys. Rev. B* **98** 014110
- [28] Fan L, He Y, Zhao X and Chen X A 2020 Subwavelength and broadband tunable topological interface state for flexural wave in one-dimensional locally resonant phononic crystal *J. Appl. Phys.* **127** 235106
- [29] Chaplain G J, De Ponti J M, Aguzzi G, Colombi A and Craster R V 2020 Topological rainbow trapping for elastic energy harvesting in graded Su-Schrieffer-Heeger systems *Phys. Rev. Appl.* **14** 054035
- [30] Zhao D, Chen X, Li P and Zhu X F 2021 Subwavelength acoustic energy harvesting via topological interface states in 1D helmholtz resonator arrays *AIP Adv.* **11** 015241
- [31] Sun C, Song A, Liu Z, Xiang Y and Xuan F Z 2023 Topological fano resonance of symmetric lamb wave induced by antisymmetric trapped mode *AIP Adv.* **13** 025008
- [32] Chen C, Chen T, Wang Y, Wu J and Zhu J 2019 Observation of topological locally resonate and Bragg edge modes in a two-dimensional slit-typed sonic crystal *Appl. Phys. Express* **12** 097001
- [33] Zhang Q, Chen Y, Zhang K and Hu G 2020 Dirac degeneracy and elastic topological valley modes induced by local resonant states *Phys. Rev. B* **101** 014101
- [34] Xu G G, Sun X W, Wen X D, Liu X X, Song T and Liu Z J 2023 Valley transport via dual-band elastic topological edge states in local-resonant phononic crystal plate *J. Appl. Phys.* **133** 095110
- [35] Fan L, Chen Y, An S, Liu T, Fan H, Zhu J and Su Z 2023 Local-resonance-induced dual-band topological corner states of flexural waves in a perforated metaplate *Phys. Rev. Appl.* **19** 034065
- [36] Dorin P, Khan M and Wang K W 2023 Uncovering and experimental realization of multimodal 3D Topological metamaterials for low-frequency and multiband elastic wave control *Adv. Sci.* **10** 2304793
- [37] Wang G, Wang T, Chen Z, Zhu Z and Lim C W 2024 A novel 3D topological metamaterial for controllability of polarization-dependent multilayer elastic waves *Composites B* **275** 111341
- [38] Lu Z Q, Zhao L, Ding H and Chen L Q 2021 A dual-functional metamaterial for integrated vibration isolation and energy harvesting *J. Sound Vib.* **509** 116251
- [39] Chaurha A, Malaji P V and Mukhopadhyay T 2022 Dual functionality of vibration attenuation and energy harvesting: effect of gradation on non-linear multi-resonator metastructures *Eur. Phys. J. Spec. Top.* **231** 1403–13
- [40] Yu D, Wen J, Shen H, Xiao Y and Wen X 2012 Propagation of flexural wave in periodic beam on elastic foundations *Phys. Lett. A* **376** 626–30
- [41] Siddiqui M A and Hawwa M A 2021 Flexural edge waves in a Kirchhoff plate carrying periodic edge resonators and resting on a winkler foundation *Wave Motion* **103** 102720
- [42] Zhang G, He Z, Wang S, Hong J, Cong Y and Gu S 2024 Elastic foundation-introduced defective phononic crystals for tunable energy harvesting *Mech. Mater.* **191** 104909
- [43] Sun Y, Han Q, Jiang T and Li C 2024 Coupled bandgap properties and wave attenuation in the piezoelectric metamaterial beam on periodic elastic foundation *Appl. Math. Modelling* **125** 293–310
- [44] Wang G, Guan Y, Chen Z, Xu X, Zhou Z and Lim C W 2023 New topological rainbow trapping approach for phononic beam-foundation systems *J. Appl. Phys.* **56** 385309
- [45] Chen Z, Wang G and Lim C W 2022 Periodically alternated elastic support induced topological phase transition in phononic crystal beam systems *Int. J. Solids Struct.* **239–240** 111461
- [46] Hu G, Lan C, Tang L and Yang Y 2022 Deep-subwavelength interface states in mechanical systems *Mech. Syst. Signal Process.* **169** 108598
- [47] Hu G, Lan C, Tang L and Yang Y 2022 Local resonator stimulated polarization transition in metamaterials and the formation of topological interface states *Mech. Syst. Signal Process.* **165** 108388
- [48] Gao N, Wang B, Lu K and Hou H 2021 Complex band structure and evanescent bloch wave propagation of periodic nested acoustic black hole phononic structure *Appl. Acoust.* **177** 107906
- [49] Jiang Y, Meng F, Chen Y, Zheng Y, Chen X, Zhang J and Huang X 2020 Vibration attenuation analysis of periodic underground barriers using complex band diagrams *Comput. Geotech.* **128** 103821
- [50] Hussein M I 2016 Wave motion in periodic flexural beams and characterization of the transition between Bragg scattering and local resonance *J. Appl. Mech.* **79** 011003
- [51] Xiao Y, Wen J, Wang G and Wen X 2013 Theoretical and experimental study of locally resonant and bragg band gaps in flexural beams carrying periodic arrays of beam-like resonators *J. Vib. Acoust.* **135** 041006
- [52] Sharma B and Sun C T 2016 Local resonance and Bragg bandgaps in sandwich beams containing periodically inserted resonators *J. Sound Vib.* **364** 133–46
- [53] Tian X, Chen W, Gao R and Liu S 2021 Merging Bragg and local resonance bandgaps in perforated elastic metamaterials with embedded spiral holes *J. Sound Vib.* **500** 116036
- [54] Xiao M, Ma G, Yang Z, Sheng P, Zhang Z Q and Chan C T 2015 Geometric phase and band inversion in periodic acoustic systems *Nat. Phys.* **11** 240–4
- [55] Čajić M, Karličić D, Christensen J and Adhikari S 2023 Tunable topological interface states in one-dimensional inerter-based locally resonant lattices with damping *J. Sound Vib.* **542** 117326
- [56] Jang Y, Kim S, Kim E and Rho J 2024 Realization of singular topological edge states in locally resonant metamaterials (arXiv:2405.13631)